A new dataset of rain cells based on observations of Tropical Rainfall Measuring Mission (TRMM) precipitation radar, visible/infrared scanner and microwave imager

Zhenhao Wu[1], Jian Shang[2], Chunguan Cui[3], Peng Zhang[2], Songyan Gu[2], and Lin Chen[2], Yunfei Fu[1]

[1]School of Earth and Space Sciences, CMA-USTC Laboratory of Fengyun Remote Sensing, University of Science and Technology of China, Hefei, 230026, China

[2]Key Laboratory of Radiometric Calibration and Validation for Environmental Satellites, National Satellite Meteorological Center, China Meteorological Administration, Beijing, 100081, China

[3]Institute of Heavy Rain, China Meteorological Administration, Wuhan, 430205, China

Correspondence: Yunfei Fu (fyf@ustc.edu.cn)

Abstract. Understanding the characteristics of the rain cell, the most basic unit in the natural precipitation system, is helpful in improving the cognition of the precipitation system. In this study, based on the merged precipitation profile data, reflectance and infrared data, and microwave brightness temperature data observed by the Tropical Rainfall Measuring Mission (TRMM) precipitation radar (PR), visible and infrared scanner (VIRS) and TRMM microwave imager (TMI), rain cells were identified in the PR swath. For the identified valid rain cells, two fitting methods (the minimum bounding rectangle (MBR) and the best fit ellipse (BFE)) were applied to fit the external frame. Then, the geometric and physical parameters of rain cells were also calculated. By analyzing the geometric parameters (length, width, height, and so on) and physical parameters (rain rate, visible reflectance and thermal infrared brightness temperature from cloud top, and microwave brightness temperature from cloud column) of two rain cells (weak rain cell and strong rain cell), the results indicate that the strong rain cell is filled with deep convective precipitation and has low thermal infrared brightness temperature at the cloud top, while the weak rain cell is mainly characterized by stratiform precipitation with low rain rate. Compared to the BFE method, the area of the external frame calculated by the MBR method is generally larger. The filling ratio of the BFE method is slightly higher than that of the MBR method. In general, the results indicate that the rain cell definition parameters using the two fitting methods are reasonable and intuitive. The data used in this paper are freely available at https://doi.org/10.5281/zenodo.15387988 (Wu and Fu, 2025).

1 Introduction

Precipitation is an important part of the global energy and water cycle (Houze, 1997; Oki and Kanae, 2006; Lau and Wu, 2010). In the water cycle, the rain cell that constitutes a precipitation system can be considered the most basic unit in different definitions. The investigation of the three-dimensional structure of rain cell is helpful to understand the thermodynamic structure and microphysical processes within precipitation systems (Houze, 1981; Zipser and Lutz, 1994; Yuter and Houze, 1995; Fu and Liu, 2001). Austin and Houze (1972) found subsynoptic scale precipitation regions that each had rather clearly definable characteristics and behavior when they studied the precipitation patterns in New England. Based on radar observations and rain gauge records, they also divided precipitation pattern into synoptic areas, large mesoscale areas, small mesoscale areas and cells. The rain cell with area of about 10 km^2 in radar echo was regarded as a single cumulus convective unit in their study (Gagin et al., 1986; Capsoni et al., 1987).

More studies were done by defining the threshold of rain cell, such as an area where rain rates were greater than a given threshold (Goldhirsh and Musiani, 1986). For example, Capsoni et al. (1987) defined rain cell as the connected region with rain rate greater than 5 $mm\ h^{-1}$ based on S-band radar observation near Milan in 1980. Awaka (1989) modified rain rate threshold to 0.4 $mm\ h^{-1}$. Meanwhile, many studies exposed the relationship between rain rate threshold and rain cell size based on ground-based radar data (Konrad, 1978; Sauvageot et al., 1999; Feral et al., 2000; Begum and Otung, 2009). Feral et al. (2000) adopted elliptic fitting method to investigate the geometric characteristics and directional distribution of rain cell. The statistical results also revealed that the major axis length was twice longer than the minor axis length and the direction distribution was uniform in the majority of the rain cells.

Since the late 1990s, observations from precipitation radar (PR), visible and infrared scanner (VIRS) and TRMM microwave imager (TMI) aboard the TRMM satellite have provided a wealth of data for systematic study of cloud and precipitation (Kummerow et al., 1998, 2000; Nesbitt et al., 2000; Viltard et al., 2000; Liu and Fu, 2001; He et al., 2006; Schumacher and Houze, 2003; Li and Fu, 2005; Liu and Fu, 2010; Fu, 2014). With the massive data observed by PR, VIRS and TMI, Nesbitt et al. (2006), Liu et al. (2007, 2008), and Liu and Zipser (2013) made spick-and-span studies in the field of rain cell identification and its parameters with elliptic fitting method. Their rain cell data were also widely used for analyzing the temporal and spatial distribution characteristics of rain cells (Zhou et al., 2013;

Yokoyama et al., 2014; Ni et al., 2015), such as the finding that line-shaped convective systems occurred more frequently over ocean, and showed higher frequency in the subtropics (Liu and Zipser, 2013). To continue revealing the characteristics of rain cell parameters, Fu et al. (2020) defined the geometric and physical parameters of rain cells, using the minimum bounding rectangle (MBR) fitting method to calculate the corresponding parameters for the rain cells identified within the PR scan width. The rain cell data generated from MBR method were applied to study the morphological characteristics of rain cells over the Tibetan Plateau in summer (Chen et al., 2021). Cai et al. (2024) adopted three methods, minimum circumscribed ellipse, minimum bounding rectangle and direct indexing area, for rain cell fitting. They also compared the geometric characteristics generated from the three methods.

However, the identified rain cell data need to include reflectance and infrared temperature observed by VIRS and microwave bright temperature measured by TMI, which will give full play to the advantages of TRMM instruments. For the above purposes, this study merges the observation data from PR, VIRS and TMI at the pixel resolution of PR, and then calculates the geometric parameters of the identified rain cells by using two fitting methods (MBR and BFE). Finally, a new dataset with precipitation parameters, visible/infrared and microwave signals of rain cells is produced. The structure of this study is as follows: Section 2 describes data and data merging methods, Section 3 introduces rain cell identification method and defines the geometric and physical parameters of rain cells, Section 4 analyzes two typical rain cells in geometric and physical parameters. Access to the datasets is introduced in Section 5, and conclusions are presented in Section 6.

2 Data

The TRMM was jointly developed by the US National Aeronautics and Space Administration (NASA) and the Japan Aerospace Exploration Agency (JAXA) and launched on November 27, 1997. The TRMM is a non-solar synchronous polar-orbiting satellite with an orbital inclination of $35°$ and observes regions between $38°$ S and $38°$ N (Simpson et al., 1996; Kummerow et al., 1998, 2000). The satellite carries five instruments: PR, VIRS, TMI, the Lightning Imaging Sensor (LIS), and the Cloud and Earth Radiant Energy Sensor (CERES). This study mainly involves the measurements of TRMM PR, VIRS, and TMI.

2.1 PR data 2A25

The PR was the first spaceborne precipitation radar onboard the TRMM. It is a single-frequency

microwave radar operating at 13.8 GHz (Kummerow et al., 1998; Kozu et al., 2001). PR scans in the cross-track direction at a scanning inclination of 17°. There are 49 pixels on each scanning line. The horizontal resolution is about 4.3 km at nadir (5.0 km after the orbital boost), and the scanning width is 215 km (245 km after the orbital boost). It can detect the three-dimensional structure of precipitation from mean sea level to 20 km (a total of 80 layers) with a vertical resolution of 0.25 km.

The 2A25 data are the second-level data product of the TRMM PR, which are generated by inverting the echo signals detected by the PR. This dataset mainly includes scanning time, geographic information, three-dimensional rain rate, rain type and so on (Awaka et al., 1997). The detection sensitivity of the PR is about 17 dBZ, corresponding to the rain rate of about 0.4 $mm\ h^{-1}$ (Schumacher and Houze, 2003). Therefore, when the rain rate of the pixels is lower than 0.4 $mm\ h^{-1}$, a default value is assigned, and those pixels are not included in the calculation.

2.2 VIRS data 1B01

The VIRS scans in the cross-track direction with a scanning angle of 45°. There are 261 pixels on each scanning line. The scanning width is 720 km (833 km after the orbital boost), and the horizontal resolution is 2.2 km at nadir (2.4 km after the orbital boost). It has five channels from the visible to the far infrared band: CH1 (0.63 μm), CH2 (1.6 μm), CH3 (3.7 μm), CH4 (10.8 μm) and CH5 (12.0 μm). The 1B01 is a first-level data product of VIRS, which includes the reflectance at CH1 and CH2, the infrared radiation brightness temperature at CH3, CH4, and CH5 after correcting and calibrating the VIRS detection results.

2.3 TMI data 1B11

The TMI is a nine-channel passive microwave radiometer with five frequencies spanning from 10 to 85 GHz. The microwave signal frequencies are 10.65 GHz, 19.35 GHz, 21.3 GHz, 37.0 GHz, and 85.5 GHz, with 21.3 GHz being a single vertical polarization channel. The other four frequencies are dual horizontal (H) and vertical (V) polarization channels. The scanning width is 760 km (878 km after the orbital boost). The horizontal resolution of each frequency channel (effective field of view of beam, Kummerow et al., 1998) varies from 63 km × 37 km at 10.65 GHz to 7 km × 5 km at 85.5 GHz. The 1B11 data contain the calibrated TMI-detected microwave brightness temperature at multiple channels.

2.4 The merged data of 2A25, 1B01 and 1B11

115   To comprehensively analyze the parameters of precipitation, cloud top spectral signal and particle phase

116   in precipitation systems, the rain rate profile and echo profile of 2A25, the reflectance and infrared

117   temperature of 1B01, and the microwave brightness temperature of 1B11 were collocated in PR

118   horizontal resolution to produce a merged dataset. The reason for that is the difference spatial resolutions

119   of the three instruments, but the time lag of observation among the three instruments to the same target

120   is less than 1 min, i.e., the quasi-synchronous observations (Liu et al., 2008; Fu et al., 2011; Sun and Fu,

121   2021). Statistics show about 7 VIRS pixels within 1 PR pixel. It was found that the spectral signals of

122   VIRS changed weakly after merging; the mean change was less than 0.7 %, and the mean square

123   deviation was less than 2.5 % (Fu et al., 2011). Because TMI channels have different spatial resolutions

124   that are larger than PR pixel resolution, the nearest neighbor method was used to obtain microwave

125   brightness temperature at PR pixel resolution, i.e., each PR pixel was assigned the microwave brightness

126   temperatures of nine channels from a TMI pixel closest to the PR pixel (Liu et al., 2008).

127   **3 Method**

128   **3.1 The algorithm of rain cell identification**

129   The definition of rain cell in this study is the same as that proposed by Fu et al. (2020), i.e., a rain cell

130   consists of at least four connected rain pixels within the swath of PR's scan. This also eliminates those

131   tiny rain cells smaller than four rain pixels. In the process of identifying rain cells, the eight-connected

132   domain method is used. According to the working mode of PR, its swath consists of 49 pixels (from

133   number 1 to 49), so if the identified rain cell has pixels at the PR swath edge (the first pixel and 49th

134   pixel), the rain cell is not included. If the identified rain cell is at the beginning or end of the PR swath,

135   the rain cell is also eliminated. The advantage of this is to avoid the truncation effect of PR swath. For

136   the identified rain cells, this study utilizes the minimum bounding rectangle (MBR) fitting method and

137   the best fit ellipse (BFE) fitting method to calculate the geometric parameters. The two methods can fit

138   an ellipse and a rectangle frame with the smallest area covering the target object (rain cell), as done by

139   Nesbitt et al. (2006) and Fu et al. (2020), respectively. There are differences in the geometric parameters

140   calculated by the MBR and BFE fitting methods, such as the area of the external frame and spatial

141   morphology index of rain cell. However, the physical parameters are unaffected by both methods. The

142   rain cell parameters calculated in this study by the two fitting methods can be used by studies according

143 to their own preferences.

3.2 The definitions of rain cell parameters

145 The definitions of geometric and physical parameters describing the identified rain cell were almost the

146 same as that of Fu et al. (2020). The specific geometric parameters are listed in Table 1, in which the first

147 six parameters describe the horizontal geometry of rain cells and the rest describe the vertical geometry.

148 These parameters have a clear physical meaning, such as α, which represents the horizontal shape of a

149 rain cell, a small (large) α indicates that the horizontal shape of rain cell is more like a strip (square)

150 precipitation system, and it has more (less) correlation with a frontal precipitation system. The variable

151 β expresses the ratio of a rain cell's area (S_{rain}) to the area of a rectangle or ellipse frame (S), and

152 characterizes the effectiveness of both methods used to fit the external frame of rain cells. A large (small)

153 β indicates a larger (smaller) number of rain pixels inside the rectangle or ellipse frame. The variables

154 γ_{max} and γ_{av} represent the three-dimensional spatial shape of a rain cell. Small γ_{max} (γ_{av}) indicates

155 a "squatty" appearance of a rain cell, in contrast to a "lanky" appearance for larger γ_{max} (γ_{av}).

156 **Table 1. Geometric parameter definitions of rain cell by the minimum bounding rectangle (MBR) method and**

157 **the best fit ellipse (BFE) method**

Parameters in MBR method	Parameters in BFE method
L_r (km), length	L_e (km), length of the major axis
W_r (km), width	W_e (km), length of the minor axis
α_r, horizontal shape index, $\alpha_r = W_r/L_r$	α_e, horizontal shape index, $\alpha_e = W_e/L_e$
S_r (km^2), MBR area, $S_r = L_r * W_r$	S_e (km^2), BFE area, $S_e = \frac{\pi}{4} * L_e * W_e$
β_r, filling ratio, $\beta_r = S_{rain}/S_r$	β_e, filling ratio, $\beta_e = S_{rain}/S_e$
S_{rain} (km^2), rain area, sum of all rain pixel areas in rain cell	
H_{max} (km), maximum echo top height in rain cell	
H_{av} (km), mean echo top height in rain cell	
γ_{max}, maximum spatial morphology index of rain cell, $\gamma_{max} = H_{max}/L$	
γ_{av}, mean spatial morphology index of rain cell, $\gamma_{av} = 2H_{av}/(L + W)$	
H_{avc} (km), mean echo top height of convective precipitation in rain cell	
H_{avs} (km), mean echo top height of stratiform precipitation in rain cell	
H_dBZ_{max} (km), height of the maximum reflectivity factor in rain cell	
μ, ratio of the maximum reflectivity factor height to the maximum echo top height in rain cell	

158 The physical parameter definitions of rain cells are listed in Table 2 including rain type, rain rate profile,

159 reflectivity factor profile, mean rain rate, visible reflectance and infrared brightness temperature,

160 microwave brightness temperature and so on. These parameters are significant for characterizing the

161 intensity, the inhomogeneity, and the evolution stage of rain cell.

162 **Table 2. Physical parameter definitions of rain cell by the minimum bounding rectangle (MBR) method and**

163 **the best fit ellipse (BFE) method.**

Sensor	Symbol	Physical meaning
PR	RR_{ave} (mm h^{-1})	Mean rain rate in rain cell
	RR_{max} (mm h^{-1})	Maximum rain rate in rain cell
	RR_{avc} (mm h^{-1})	Mean convective rain rate in rain cell
	RR_{avs} (mm h^{-1})	Mean stratiform rain rate in rain cell
	RR_{maxc} (mm h^{-1})	Maximum rain rate of convective precipitation in rain cell
	RR_{maxs} (mm h^{-1})	Maximum rain rate of stratiform precipitation in rain cell
	CAF (%)	Convective area fraction to total precipitation area in rain cell
	SAF (%)	Stratiform area fraction to total precipitation area in rain cell
	CPC (%)	Convective precipitation contribution to total precipitation in rain cell
	SPC (%)	Stratiform precipitation contribution to total precipitation in rain cell
	dBZ_{max} (dBZ)	Maximum reflectivity factor in rain cell
VIRS	RF_{ave}	Mean reflectance of visible or near infrared channel in rain cell
	RF_{avc}	Mean reflectance of visible or near infrared channel for convective precipitation in rain cell
	RF_{avs}	Mean reflectance of visible or near infrared channel for stratiform precipitation in rain cell
VIRS/TMI	TB_{ave} (K)	Mean brightness temperature of sensor channel in rain cell
	TB_{avc} (K)	Mean brightness temperature of sensor channel for convective precipitation in rain cell
	TB_{avs} (K)	Mean brightness temperature of sensor channel for stratiform precipitation in rain cell

164 **4 Results**

165 **4.1 Precipitation parameters of rain cell**

166 In order to better understand the geometric and physical parameters of rain cells using the MBR and BFE

167 fitting methods, two rain cells are analyzed below. One identified rain cell A occurred on 2 June 1999 in

168 the southern Tibetan Plateau (TRMM orbit 08691), and the other, rain cell B, on 13 June 2003 in the

169 eastern Tibetan Plateau (TRMM orbit 31787). Figure 1 shows the distribution of rain rate and rain type

170 for the two rain cells. The frames of both methods are also plotted, which clearly shows the length and

171 width of the frame from the MBR fitting method, and the long and short axes of the frame from the BFE

172 fitting method. Table 3 lists the statistics of parameters for the two rain cells. Figure 1a shows that rain

173 cell A applying the MBR fitting method has length 291.25 km (L_r), width 140.68 km (W_r), rain area

174   10223.50 km^2 (S_{rain}), MBR area 40971.84 km^2 (S_r), and filling ratio 0.25 (β_r). The horizontal shape

175   index is 0.48 (α_r), which indicates rain cell A with a strip like shape. The rain cell A applying the BFE

176   fitting method (Figure 1c) has length 345.88 km (L_e), width 144.08 km (W_e), rain area 10223.50 km^2

177   (S_{rain}), BFE area 39140.42 km^2 (S_e), and filling ratio 0.26 (β_e). The horizontal shape index is 0.42 (α_e),

178   which also indicates rain cell A with a strip like shape. Rain cell B, shown in Figures 1b and 1d applying

179   the MBR and BFE fitting method, has parameters listed in Table 3 that show it is slightly strip-shape.

180   The vertical parameters of both rain cells are also listed in Table 3. The variables γ_{max} and γ_{av} are

181   affected by the fitting method. Comparing rain cell A and B, the latter has higher echo tops (H_{max} =

182   17.75 km, H_{av} = 9.47 km), and shows a "lanky" appearance (γ_{max} = 0.11, γ_{av} = 0.08 in the MBR

183   fitting method; γ_{av} = 0.07 in the BFE fitting method). In rain cell B, the mean echo top height of

184   convective precipitation (10.39 km) and stratiform precipitation (7.96 km) is also higher than those in

185   rain cell A (H_{avc} = 5.76 km, H_{avs} = 5.58 km), which indicates that rain cell B has stronger updraft

186   velocity and a deeper precipitating cloud. The ratio of the maximum reflectivity factor height to the

187   maximum echo top height, μ, is 0.37 and 0.15 for rain cell A and B, respectively. By combining γ_{max}

188   and μ, it can be concluded that rain cell B is a deep precipitation system with large particles in the lower

189   part of the cloud.
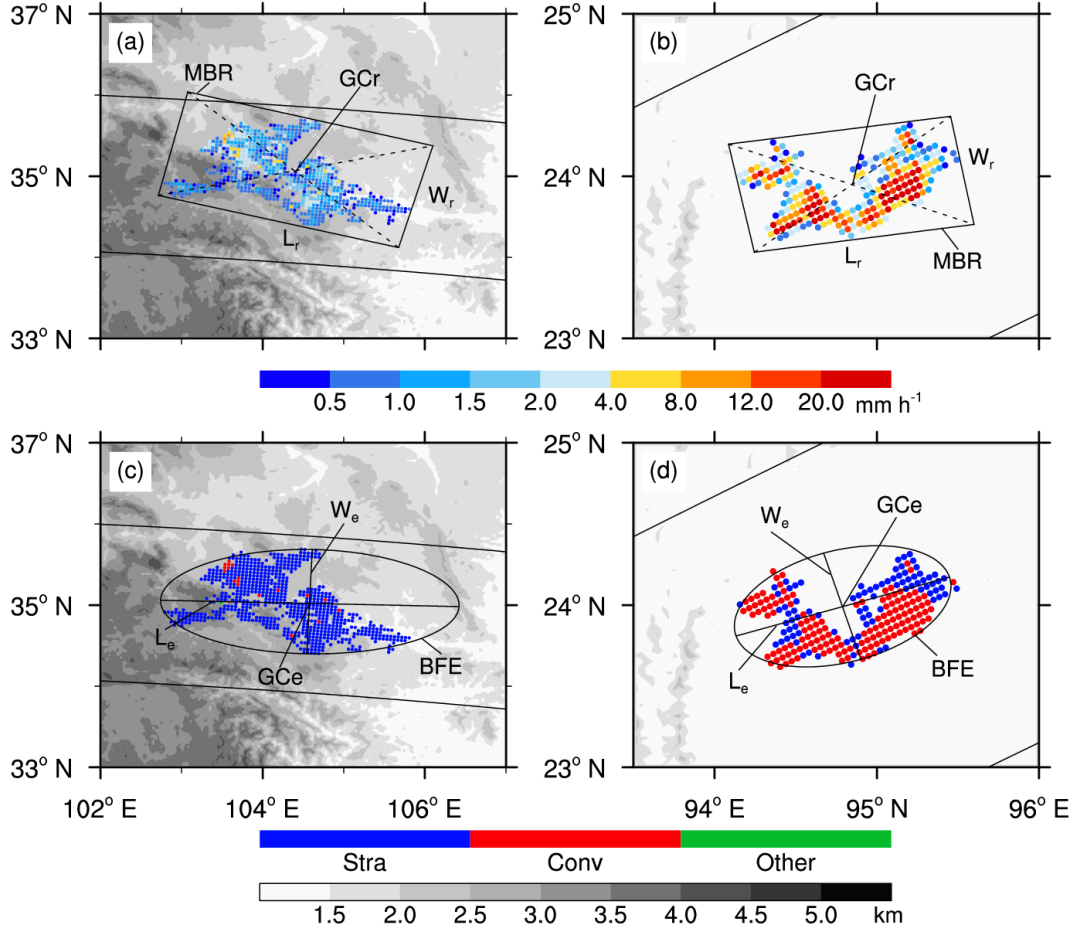
Figure 1. Two rain cells occurred on June 2, 1999 and June 13, 2003 measured by PR: rain rate (a and b) and rain type (c and d, blue, red and green represent for stratiform, convective and other precipitation, respectively). The two rain cells in up panel were identified by MBR method, in bottom by BFE method. GCr and GCe represent for geometric center of rain cell identified by MBR method and BFE method, respectively. The gray level in the figure represents the elevation of the terrain.

The physical parameters of both rain cells are listed in Table 4. PR observation shows that the mean rain rate RR_{ave} and the maximum rain rate RR_{max} of rain cell B are 11.64 $mm\,h^{-1}$ and 113.14 $mm\,h^{-1}$, respectively, while rain cell A is a relatively weak rain cell. The defined physical parameters also show that the mean convective rain rate of rain cell A is 5.52 $mm\,h^{-1}$, and that of rain cell B is 17.35 $mm\,h^{-1}$. Meanwhile, the mean stratiform rain rate of rain cell A and rain cell B are 1.16 $mm\,h^{-1}$ and 2.31 $mm\,h^{-1}$, respectively. The convective area fraction to total precipitation area (CAF) and stratiform area fraction to total precipitation area (SAF) are 2.56% and 97.3% for rain cell A, and 62.01% and 37.99% for rain cell B, respectively. The convective precipitation contribution to total precipitation (CPC) and stratiform precipitation contribution to total precipitation (SPC) are 11.14% and 88.79% for rain cell A, and 92.46% and 7.54% for rain cell B, respectively. This indicates that rain cell B is a

206 convective rain cell while rain cell A is a stratiform rain cell. Rain cell B reaches the maximum reflectivity

207 factor at an altitude of 2.75 km, while rain cell A reaches its maximum at 3.25 km. However, the dBZ_{max}

208 of rain cell B is 57.81 dBZ, which is much higher than that of rain cell A (36.38 dBZ). This reflects that

209 there are relatively large particles at the bottom of rain cell B in the cloud.

210 **Table 3. The geometric parameters of rain cell A and B calculated by MBR method and BFE method.**

MBR method		BFE method	
L_r (km)	291.25/170.49	L_e (km)	345.88/174.84
W_r (km)	140.68/77.11	W_e (km)	144.08/83.94
α_r	0.48/0.45	α_e	0.42/0.48
S_r (km^2)	40971.84/13145.87	S_e (km^2)	39140.42/11526.50
β_r	0.25/0.34	β_e	0.26/0.39
γ_{max}	0.03/0.10	γ_{max}	0.03/0.10
γ_{av}	0.03/0.08	γ_{av}	0.02/0.07
S_{rain} (km^2)		10223.50/4496.40	
H_{max}(km)		8.75/17.75	
H_{av} (km)		5.59/9.47	
H_{avc} (km)		5.76/10.39	
H_{avs} (km)		5.58/7.96	
H_dBZ_{max} (km)		3.25/2.75	
μ		0.37/0.15	

211

212 **Table 4. The physical parameters of rain cell A and B calculated by MBR method and BFE method.**

Sensor	Physical parameter		Sensor	Physical parameter	
PR	RR_{ave} (mm h^{-1})	1.27/11.64	VIRS	$RF1_{ave}$	0.72/0.69
	RR_{max} (mm h^{-1})	8.08/113.14		$RF1_{avc}$	0.73/0.66
	RR_{avc} (mm h^{-1})	5.52/17.35		$RF1_{avs}$	0.72/0.73
	RR_{avs} (mm h^{-1})	1.16/2.31		$TB_{10.8\_ave}$ (K)	253.65/222.96
	RR_{maxc} (mm h^{-1})	8.08/113.14		$TB_{10.8\_avc}$ (K)	252.42/221.51
	RR_{maxs} (mm h^{-1})	4.45/11.87		$TB_{10.8\_avs}$ (K)	253.68/225.31
	CAF (%)	2.56/62.01	TMI	$TB_{19GHz\_H\_ave}$ (K)	260.61/276.75
	SAF (%)	97.3/37.99		$TB_{19GHz\_H\_avc}$ (K)	258.38/275.79
	CPC (%)	11.14/92.46		$TB_{19GHz\_H\_avs}$ (K)	260.66/278.32
	SPC (%)	88.79/7.54		$TB_{85GHz\_H\_ave}$ (K)	254.44/219.11
	dBZ_{max} (dBZ)	36.38/57.81		$TB_{85GHz\_H\_avc}$ (K)	252.84/212.72
				$TB_{85GHz\_H\_avs}$ (K)	254.49/229.53

213 **4.2 VIRS and TMI signals of rain cell**

214 Since TRMM PR, VIRS, and TMI observed the same target in spatiotemporal synchronization, the spatial

215 distributions of visible reflectance (0.63 μm) and far-infrared brightness temperature (10.8 μm) for the

216   two rain cells are shown in Figure 2. The figure also shows the external frames of rain cells using the

217   MBR and BFE fitting methods. It indicates many strips of reflectance (larger than 0.8) and a uniform

218   distribution of brightness temperature (varying from 240 to 250 K) for rain cell A, while rain cell B

219   consists of two convective clouds with reflectance greater than 0.85 and brightness temperature lower

220   than 220 K. Table 4 also shows the calculated mean visible reflectance $RF1_{ave}$ for the two rain cells

221   (0.72 for rain cell A and 0.69 for rain cell B, respectively). The $RF1_{avc}$ ($RF1_{avs}$) for rain cell A is 0.73

222   (0.72), and for rain cell B, it is 0.66 (0.73). The large reflectance values indicate that the cloud optical

223   thickness at the top of the two rain cells is large. The mean brightness temperature at VIRS channel 10.8

224   μm ($TB_{10.8\_ave}$) is 253.65 K and 222.96 K for the two rain cells, indicating that rain cell B has a higher

225   cloud top, i.e., the ice phase is distributed at the cloud top, while the cloud top of rain cell A has an ice-

226   liquid mixed phase. The values of $TB_{10.8\_avc}$ are lower than those of $TB_{10.8\_avs}$, which indicates that

227   the cloud top height of convective rain pixels is higher than that of stratiform rain pixels. The signals of

228   VIRS channels can be used to retrieve cloud parameters. The retrieval algorithms have been studied and

229   reviewed by many authors (Nakajima and King, 1990; Rossow and Garder, 1993; Han et al., 1994;

230   Rossow and Schiffer, 1999; Fu, 2014). In addition, the relationship between the precipitation of PR and

231   the brightness temperature of VIRS can be extended to the infrared brightness temperature of

232   geostationary satellites, thereby improving the precipitation forecasting capability of geostationary

233   satellites.
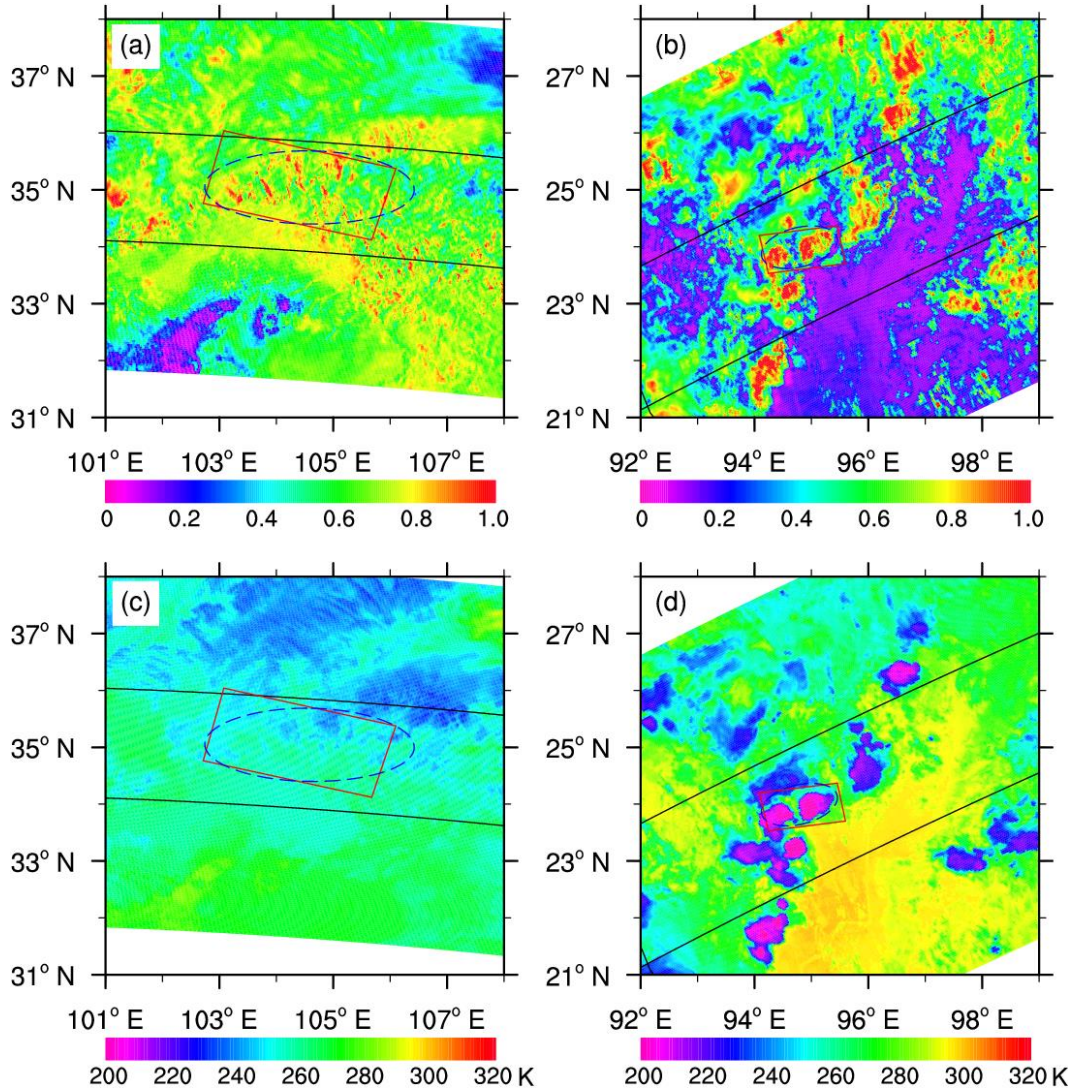
Figure 2. The reflectance distribution of visible channel at 0.63 μm (a and b) and brightness temperature distribution of far-infrared channel at 10.8 μm (c and d) for the two cases observed by VIRS (Visible and Infrared Scanner). The solid black line is PR (Precipitation Radar) scanning track. The red solid rectangle and blue dash ellipse represent for the area of rain cell identified by MBR method and BFE method, respectively.

Similar to Figure 2, the distribution of microwave brightness temperature observed by nine channels of TMI is shown. However, for simplicity, Figure 3 only plots the distribution of brightness temperature at the TMI horizontal polarization channels 19.4 GHz and 85 GHz. At channel 19.4 GHz, rain cell A shows relatively lower brightness temperature (from 250 to 280 K), while rain cell B has higher brightness temperature (from 260 to 290 K). Because the low-frequency microwave channel is easily affected by the radiation from the land surface, it can be judged that the temperature of land surface in rain cell A is lower than that in rain cell B. The brightness temperature of microwave high frequency channels is mainly affected by the composition of ice phase inside cloud, such as ice particles and

248   supercooled water, while the influence of land surface radiation on these channels is weak. The more

249   content of ice phase composition inside the cloud, the lower brightness temperature at these high

250   frequency channels. According to this principle, rain cell B shows low brightness temperature at 85 GHz

251   in Figure 3d because the rain cell belongs to a deep convective precipitation system. Because rain cell A

252   has more stratiform precipitation and fewer ice particles, its brightness temperature at the same channel

253   is higher. In Table 4, the mean brightness temperature at channel 19.4 GHz and 85 GHz also indicates

254   the difference between the two rain cells and between the two rain types. The microwave brightness

255   temperature of TMI channels can be used to retrieve cloud parameters such as ice water, liquid water, or

256   rain rate based on retrieval algorithms of previous studies (Grody, 1976; Grody et al., 1980; Liu and

257   Curry, 1993; Petty, 1994a, 1994b; Wang et al., 2009; Fu, 2021). The rain rate from PR can also help

258   optimize the passive microwave inversion of precipitation results. The related algorithms can be extended

259   to the same microwave instruments on different platforms in the future.
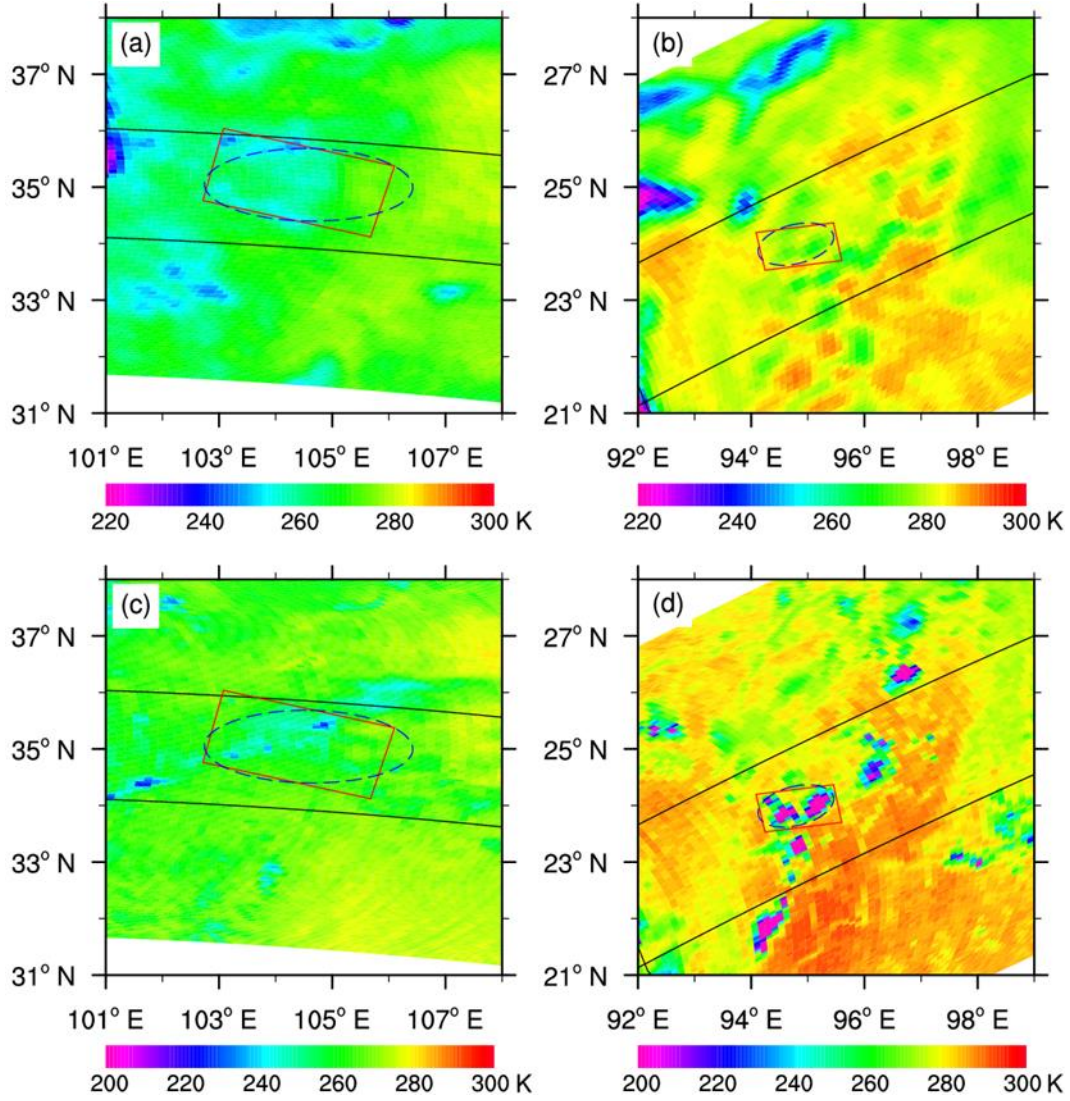
Figure 3. The brightness temperature distribution of microwave horizontal polarization channel at 19 GHz (a and b) and at 85 GHz (c and d) for the two cases observed by TMI (TRMM Microwave Imager). The solid black line is PR (Precipitation Radar) scanning track. The red solid rectangle and blue dash ellipse represent for the area of rain cell identified by MBR method and BFE method, respectively.

In order to visually display the parameter distributions of rain cells A and B using the MBR and BFE fitting methods, Figure 4 shows the distribution of rain rate, reflectance at VIRS visible channel, brightness temperature at VIRS thermal infrared channel, and microwave brightness temperatures at TMI low-frequency and high-frequency channels. It must be pointed out that both VIRS and TMI signals in Figure 4 correspond to PR precipitation pixels (that is, signals corresponding to each PR pixel's resolution), and these signals are not provided if no precipitation exists in the rain cell. Therefore, the rain cell data established in this study facilitate the study of the relationships among precipitation, visible/infrared, and microwave signals. The combination of multi-source data can effectively enhance

273 the understanding of precipitation systems.

274   A simple application is shown in Figure 5, which displays the multi-parameter distribution along the

275 AB line and EF line in Figure 4a and 4b, respectively. The vertical cross sections of reflectivity factor

276 (Figure 5a and 5b) show that rain cell A is a shallow and weak precipitation system, while rain cell B is

277 deep convective precipitation system. The strong echo (greater than 38 dBZ) of rain cell B reaches higher

278 altitude, nearly 16 km. The visible reflectance (Figure 5c and 5d) from the cloud tops of the two rain

279 cells varies between 0.4 and 0.8, and the reflectance of the strong echo region in rain cell B is higher

280 (greater than 0.6). The near-infrared reflectance (Figure 5c and 5d) varies from 0.1 to 0.4, which means

281 there are a lot of ice particles inside the cloud of the two rain cells. The infrared brightness temperature

282 at VIRS channel 3.7 μm (Figure 5e and 5f) shows higher values in rain cell A, relatively lower in rain

283 cell B. At VIRS channels 10.8 μm and 12.0 μm, rain cell A has uniform brightness temperatures, while

284 rain cell B exhibits the characteristics of a deep convective cloud top, with low brightness temperature.

285 For the four horizontal polarization channels of TMI (Figures 5i and 5j), the microwave brightness

286 temperature of rain cell A is uniformly distributed, and the brightness temperature of each channel has

287 little difference. In rain cell B, the brightness temperature at low-frequency channels, 10 GHz and 19

288 GHz, is also evenly distributed, and the brightness temperature at the two channels is higher than that in

289 rain cell A, but the brightness temperature at the 37 GHz and 85 GHz channels changes significantly.

290 Corresponding to the strong echo region in Figure 5b, the brightness temperature of these two channels

291 is low, indicating that there are more ice particles inside the cloud in strong echo region of rain cell B.

292 The results indicate that the established new data can be used to analyze the spectral signals and

293 microwave characteristics of precipitating clouds.
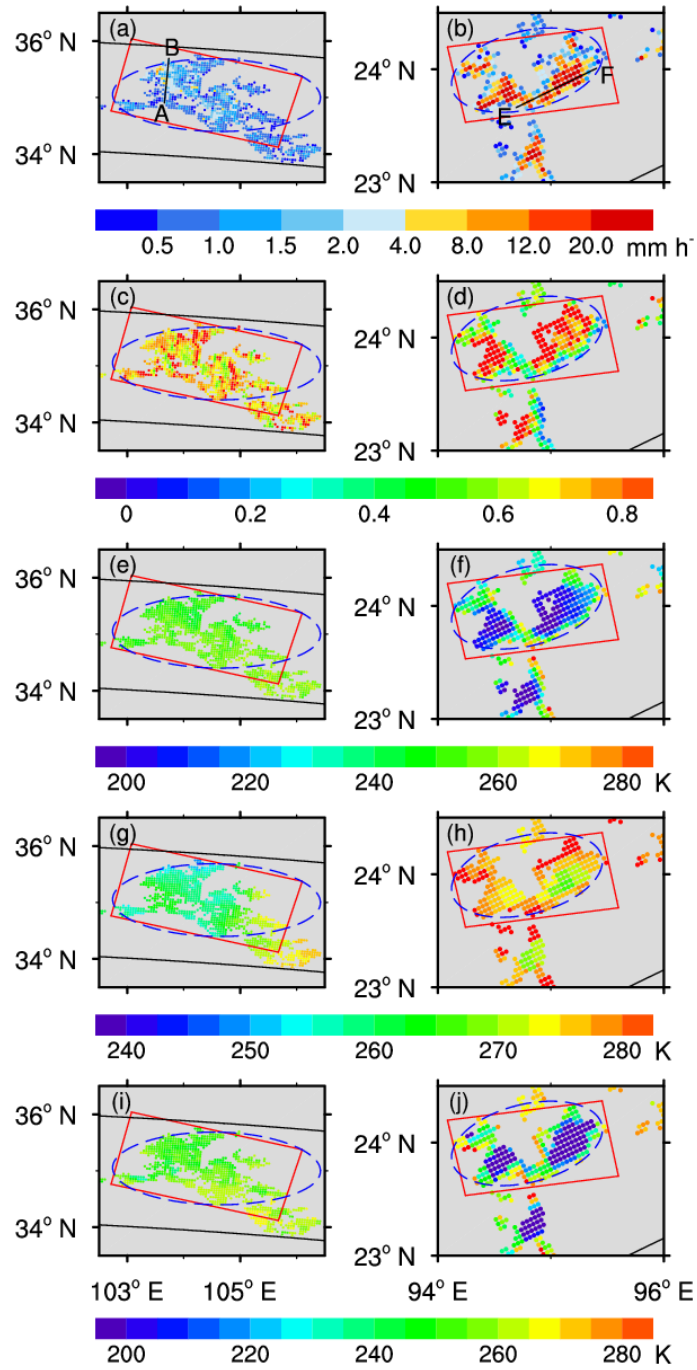
294
295 **Figure 4. The distributions of near-surface rain rate (a and b), reflectance at channel 0.63 μm (c and d),**
296 **brightness temperature at far-infrared channel 10.8 μm (e and f), brightness temperature at horizontal**
297 **channel 19 GHz (g and h) and at 85 GHz (i and j) for the two cases based on the merged data.**

298
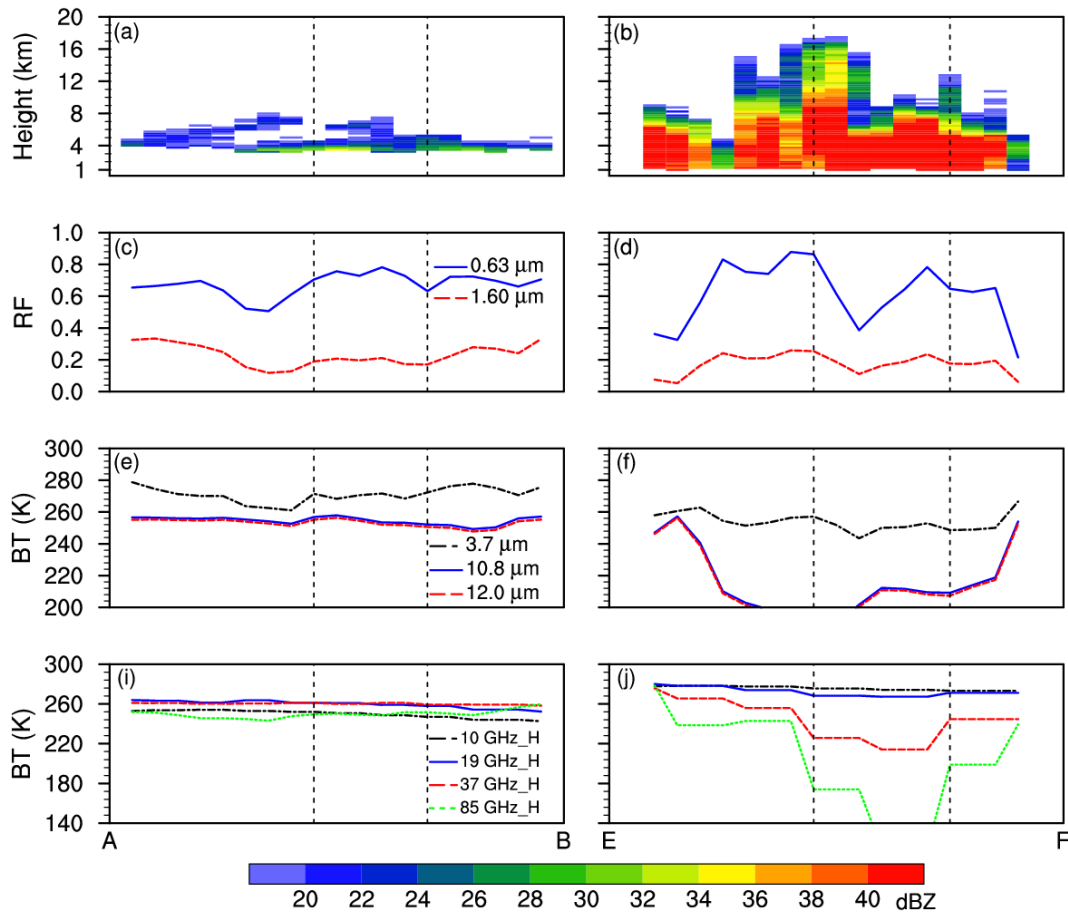
299 **Figure 5. The vertical cross sections of reflectivity factor (a and b), reflectance at VIRS channel 0.63 μm and**

300 **1.60 μm (c and d), infrared brightness temperature at VIRS channel 3.7 μm, 10.8 μm and 12.0 μm (e and f),**

301 **microwave brightness temperature at TMI horizontal channel 10 GHz, 19 GHz, 37 GHz and 85 GHz along**

302 **AB line and EF line as shown in Figure 4a and 4b.**

303 **5 Data availability**

304 The rain cell dataset used in this study, which applies the fitting methods of MBR and BFE together with

305 the defined geometric and physical parameters to describe rain cell characteristics, is accessible at

306 https://doi.org/10.5281/zenodo.15387988 (Wu and Fu, 2025).

307 **6 Conclusions**

308 In order to study the characteristics of geometric and physical parameters of rain cells, the basic units in

309 natural precipitation systems, this study was inspired by earlier studies and made full use of the

310 advantages of TRMM PR, VIRS, and TMI observations, i.e., the precipitation profile of PR reflecting

311 precipitation structure, the visible and infrared signals of VIRS representing cloud top information, and

312 the microwave signals of TMI reflecting hydrometeors in cloud columns. By matching and merging these

313   data at PR pixels, the minimum bounding rectangle (MBR) fitting method and the best fit ellipse (BFE)

314   fitting method were applied to calculate the geometric parameters of rain cells. Thus, combining these

315   with physical parameters, a new rain cell dataset was established.

316   In this study, the geometric parameters (length, width, height, etc.) and physical parameters (rain rate,

317   visible reflectance and thermal infrared brightness temperature from cloud top, and microwave

318   brightness temperature from cloud column) of the two rain cells (weak and strong rain cells) using the

319   MBR and BFE fitting methods were calculated. The results show that the weak rain cell shows stratiform

320   precipitation with low rain rate, while the strong rain cell exhibits vertically deep convective precipitation

321   and has low thermal infrared brightness temperature at the cloud top. All these indicate that the rain cell

322   definition parameters using the two fitting methods are reasonable and intuitive.

323   It must be noted that the difference between the MBR fitting method and the BFE fitting method is

324   only in the geometric parameters of the rain cell, and the difference is minor, such as slight differences

325   in the area of the external frame of the rain cell, as well as the spatial morphology index of the rain cell.

326   The physical parameters of the rain cell are not affected by the fitting method.

327   The new rain cell data in this study can be used to study the characteristics of the geometric and

328   physical parameters of rain cells. Although a lot of achievements have been made in this field, a

329   systematic and in-depth analysis is still needed, such as the regional differences of these parameters and

330   the characteristics of climate change. It can also be used to analyze the relationship between the physical

331   and geometric parameters of rain cells, and this relationship exhibits regional differences. The effective

332   radius of cloud particles, optical thickness, liquid water path, and other parameters in rain cells can be

333   obtained by combining retrieval algorithms of visible and near-infrared reflectance. These parameters

334   can be used to analyze the characteristics of cloud physical parameters in rain cells. Parameters such as

335   cloud water and ice water in column, cloud temperature, and rain rate in rain cells can also be retrieved

336   using microwave brightness temperature retrieval algorithms, and the relationships among these

337   parameters can be analyzed. The previously mentioned studies are expected to yield results shortly.

338

339   **Author contribution.** ZW and YF prepared the data in the standardized format. ZW uploaded the data

340   in the data repository and prepared the manuscript with contribution from YF. All the authors discussed

341   the concepts and edited the manuscript.

342

Competing interests. The authors declare that they have no conflict of interest.

344

Acknowledgements. We would like to acknowledge the National Aeronautics and Space Administration (NASA) for providing TRMM PR, VIRS and TMI datasets.

347

Financial support. This research has been supported by the National Natural Science Foundation of China (grant nos. 42230612 and 42275140) and The Second Tibetan Plateau Scientific Expedition and Research (STEP) program (grant no. 2019QZKK0104)

351

References

Austin, P. M. and Houze, R. A.: Analysis of the structure of precipitation patterns in New England, J. Appl. Meteorol., 11, 926–935, https://doi.org/10.1175/1520-0450(1972)011<0926:Aotsop>2.0.Co;2, 1972.

Awaka, J.: A three-dimensional rain cell model for the study of interference due to hydrometeor scattering, J. Commun. Res. Lab., 36, 13–44, 1989.

Awaka, J., Iguchi, T., Kumagai, H., and Okamoto, K.: Rain type classification algorithm for TRMM precipitation radar, IEEE International Geoscience and Remote Sensing Symposium Proceedings. Remote Sensing – A Scientific Vision for Sustainable Development, Singapore, 3–8 August 1997, https://doi.org/10.1109/IGARSS.1997.608993, 1997.

Begum, S. and Otung, I. E.: Rain cell size distribution inferred from rain gauge and radar data in the UK, Radio. Sci., 44, RS2015, https://doi.org/10.1029/2008RS003984, 2009.

Cai, H. K., Mao, Y. Q., Zhu, X. H., Fu, Y. F., and Zhou, R. J.: Comparison of the minimum bounding rectangle and minimum circumscribed ellipse of rain cells from TRMM, Adv. Atmos. Sci., 41, 484–499, https://doi.org/10.1007/s00376-023-2281-9, 2024.

Capsoni, C., Fedi, F., Magistroni, C., Paraboni, A., and Pawlina, A.: Data and theory for a new model of the horizontal structure of rain cells for propagation applications, Radio. Sci., 22, 395–404, https://doi.org/10.1029/RS022i003p00395, 1987.

Chen, Y. L., Zhang, A. Q., Fu, Y. F., Chen, S. M., and Li, W. B.: Morphological characteristics of precipitation areas over the Tibetan Plateau measured by TRMM PR, Adv. Atmos. Sci., 38(4), 677–689, https://doi.org/10.1007/s00376-020-0233-1, 2021.

Han, Q., Rossow, W. B., and Lacis, A. A.: Near-global survey of effective droplet radii in liquid water clouds using ISCCP data, J. Climate, 7, 465–497, https://doi.org/10.1175/1520-0442(1994)007<0465:NGSOED>2.0.CO;2, 1994.

Feral, L., Mesnard, F., Sauvageot, H., Castanets, L., and Lemorton, J.: Rain cells shape and orientation distribution in south-west of France, Phys. Chem. Earth B: Hydrol. Oceans Atmos., 25, 1073–1078, https://doi.org/10.1016/s1464-1909(00)00155-6, 2000.

Fu, Y. F.: Cloud parameyers retrieved by the bispectral reflectance algorithm and associated applications, J. Meteorol. Res-Prc., 28, 965–982, https://doi.org/10.1007/s13351-014-3292-3, 2014 (in Chinese).

Fu, Y. F.: Research progress on retrieval algorithms of cloud liquid water over ocean based on remote sensing by satellite-borne passive microwave instruments, Torrential Rain and Disasters, 40, 217–230, https://doi.org/10.3969/j.issn.1004-9045.2021.03.001, 2021 (in Chinese).

Fu, Y. F., Chen, Y., Zhang, X., Wang, Y., Li, R., Liu, Q., Zhong, L., Zhang, Q., and Zhang, A.: Fundamental characteristics of tropical rain cell structures as measured by TRMM PR, J. Meteorol. Res-Prc., 34, 1129–1150, https://doi.org/10.1007/s13351-020-0035-5, 2020.

Fu, Y. F. and Liu, G. S.: The variability of tropical precipitation profiles and its impact on microwave brightness temperatures as inferred from TRMM data, J. Appl. Meteorol., 40, 2130–2143, https://doi.org/10.1175/1520-0450(2001)040<2130:Tvotpp>2.0.Co;2, 2001.

Fu, Y. F., Liu, P., Liu, Q., Ma, M., Sun, L., and Wang, Y.: Climatological Characteristics of VIRS Channels for Precipitating Cloud in Summer Over the Tropics and Subtropics, J. Atmos. Environ. Optics., 6, 129–140, https://doi.org/10.3969/j.issn.1673- 6141.2011.02.009, 2011 (in Chinese).

Gagin, A., Rosenfeld, D., Woodley, W. L., and Lopez, R. E.: 1986: Results of seeding for dynamic effects on rain-cell properties in FACE-2, J. Appl. Meteor. Climatol., 25, 3–13, https://doi.org/10.1175/1520-0450(1986)025<0003:ROSFDE>2.0.CO;2, 1986.

Goldhirsh, J. and Musiani, B.: Rain cell size statistics derived from radar observations at Wallops Island, Virginia, IEEE T. Geosci. Remote. Sens., GE-24, 947–954, https://doi.org/10.1109/TGRS.1986.289711, 1986.

Grody, N. C.: Remote sensing of atmospheric water content from satellites using microwave radiometry, IEEE T. Antenn. Propag., 24, 155–162, https://doi.org/10.1109/TAP.1976.1141324, 1976.

Grody, N. C., Grubel, A., and Shen, W. C.: Atmospheric water content over the tropical Pacific derived from the Nimbus-6 scanning microwave spectrometer, J. Appl. Meteor., 19, 986–996, https://doi.org/10.1175/1520-0450(1980)019<0986:AWCOTT>2.0.CO;2, 1980.

He, H. Z., Cheng, M. H., and Zhou, F. X.: 3D structure of rain and cloud hydrometeors for Typhoon Kujira (0302), Chinese J. Atmos. Sci., 30, 491–503, https://doi.org/ 10.3878/j.issn.1006-9895.2006.03.12, 2006 (in Chinese).

Houze, R. A.: Structures of atmospheric precipitation systems: A global survey, Radio. Sci., 16, 671–689, https://doi.org/10.1029/RS016i005p00671, 1981.

Houze, R. A.: Stratiform Precipitation in Regions of Convection: A Meteorological Paradox?, B. Am. Meteorol. Soc., 78, 2179–2196, https://doi.org/10.1175/1520- 0477(1997)078<2179:SPIROC>2.0.CO;2, 1997.

Konrad, T. G.: Statistical models of summer rainshowers derived from fine-scale radar observations, J. Appl. Meteorol., 17, 171–188, https://doi.org/10.1175/1520-0450(1978)017<0171:SMOSRD>2.0.Co;2, 1978.

Kozu, T., Kawanishi, T., Kuroiwa, H., Oikawa, M., Kumagai, H., Okamoto, K., Okumura, M., Nakatsuka, H., and Nishikawa, K.: Development of precipitation radar onboard the Tropical Rainfall Measuring Mission (TRMM) satellite., IEEE T. Geosci. Remote. Sens., 39, 102–116, https://doi.org/10.1109/36.898669, 2001.

Kummerow, C., Barnes, W., Kozu, T., Shiue, J., and Simpson, J.: The Tropical Rainfall Measuring Mission (TRMM) Sensor Package, J. Atmos. Ocean. Tech., 15, 809–817, https://doi.org/10.1175/1520-0426(1998)015<0809:TTRMMT>2.0.Co;2, 1998.

Kummerow, C., Simpson, J., Thiele, O., Barnes, W., Chang, A. T. C., Stocker, E., Adler, R. F., Hou, A., Kakar, R., Wentz, F., Ashcroft, P., Kozu, T., Hong, Y., Okamoto, K., Iguchi, T., Kuroiwa, H., Im, E., Haddad, Z., Huffman, G., Ferrier, B., Olson, W. S., Zipser, E., Smith, E. A., Wilheit, T. T., North, G., Krishnamurti, T., and Nakamura, K.: The Status of the Tropical Rainfall Measuring Mission (TRMM) after two years in orbit, J. Appl. Meteorol. Climatol., 39, 1965–1982, https://doi.org/10.1175/1520-0450(2001)040<1965:Tsottr>2.0.Co;2, 2000.

428 Lau, K. M. and Wu, H. T.: Characteristics of precipitation, cloud, and latent heating associated with the

429 Madden-Julian oscillation, J. Climate, 23, 504–518, https://doi.org/10.1175/2009jcli2920.1, 2010.

430 Li, R. and Fu, Y. F.: Tropical precipitation estimated by GPCP and TRMM PR observations, Adv. Atmos.

431 Sci., 22, 852–864, https://doi.org/10.1007/BF02918685, 2005.

432 Liu, C. T., Zipser, E. J., and Nesbitt, S. W.: Global distribution of tropical deep convection: different

433 perspectives from TRMM infrared and radar data, J. Climate, 20, 489–

434 503, https://doi.org/10.1175/JCLI4023.1, 2007.

435 Liu, C. T., Zipser, E. J., Cecil, D. J., Nesbitt, S. W., and Sherwood, S.: A cloud and precipitation feature

436 database from nine years of TRMM observations, J. Appl. Meteorol. Climatol., 47, 2712–2728,

437 https://doi.org/10.1175/2008jamc1890.1, 2008.

438 Liu, C. T. and Zipser, E. J.: Regional variation of morphology of organized convection in the tropics and

439 subtropics, J. Geophys. Res.-Atmos., 118, 453–466, https://doi.org/10.1029/2012JD018409, 2013.

440 Liu, G. S. and Curry, J. A.: Determination of characteristic features of cloud liquid water from satellite

441 microwave measurements, J. Geophys. Res., 98, 5069–5092, https://doi.org/10.1029/92JD02888, 1993.

442 Liu, G. S. and Fu, Y. F.: The characteristics of tropical precipitation profiles as inferred from satellite

443 radar measurements, J. Meteor. Soc. Japan, 79, 131–143, https://doi.org/10.2151/jmsj.79.131, 2001.

444 Liu, Q. and Fu, Y. F.: Comparison of radiative signals between precipitating and non-precipitating clouds

445 in frontal and typhoon domains over East Asia, Atmos. Res., 96, 436–446,

446 https://doi.org/10.1016/j.atmosres.2010.02.003, 2010.

447 Nakajima, T. and King, M. D.: Determination of the optical thickness and effective particle radius of

448 clouds from reflected solar radiation measurements. Part I: Theory, J. Atmos. Sci., 47, 1878–

449 1893, https://doi.org/10.1175/1520-0469(1990)047<1878:DOTOTA>2.0.CO;2, 1990.

450 Nesbitt, S. W., Cifelli, R., and Rutledge, S. A.: Storm morphology and rainfall characteristics of TRMM

451 precipitation features, Mon. Wea. Rev., 134, 2702–2721, https://doi.org/10.1175/MWR3200.1, 2006.

452 Nesbitt, S. W., Zipser, E. J., and Cecil, D. J.: A census of precipitation features in the tropics using TRMM:

453 Radar, ice scattering, and lightning observations, J. Climate, 13, 4087–4106,

454 https://doi.org/10.1175/1520-0442(2000)013<4087:ACOPFI>2.0.Co;2, 2000.

455 Ni, X., Liu, C., Zhang, Q., and Cecil, D. J.: Properties of hail storms over China and the United States

456 from the Tropical Rainfall Measuring Mission, J. Geophys. Res.-Atmos., 121, 12031–12044,

https://doi.org/10.1002/2016JD025600, 2016.

Oki, T. and Kanae, S.: Global hydrological cycles and world water resources, Science, 313, 1068–1072, https://doi.org/10.1126/science.1128845, 2006.

Petty, G.W.: Physical retrievals of over-ocean rain rate from multichannel microwave imagery. Part I: Theoretical characteristics of normalized polarization and scattering indices, Meteorl. Atmos. Phys., 54, 79–99, https://doi.org/10.1007/BF01030053, 1994a.

Petty, G.W.: Physical retrievals of over-ocean rain rate from multichannel microwave imagery. Part II: Algorithm implementation, Meteorl. Atmos. Phys., 54, 101–121, https://doi.org/10.1007/BF01030054, 1994b.

Rossow, W. B. and Garder, L. C.: Cloud detection using satellite measurements of infrared and visible radiances for ISCCP, J. Climate, 6, 2341–2369, https://doi.org/10.1175/1520-0442(1993)006<2341:CDUSMO>2.0.CO;2. 1993.

Rossow, W. B. and Schiffer, R. A.: Advances in understanding clouds from ISCCP, Bull. Amer. Meteor. Soc., 80, 2261–2288, https://doi.org/10.1175/1520-0477(1999)080<2261:AIUCFI>2.0.CO;2, 1999.

Sauvageot, H., Mesnard, F., and Tenório, R. S.: The relation between the area-average rain rate and the rain cell size distribution parameters, J. Atmos. Sci., 56, 57–70, https://doi.org/10.1175/1520-0469(1999)056<0057:TRBTAA>2.0.Co;2, 1999.

Schumacher, C. and Houze, R. A.: The TRMM precipitation radar's view of shallow, isolated rain, J. Appl. Meteorol., 42, 1519–1524, https://doi.org/10.1175/1520-0450(2003)042<1519:TTPRVO>2.0.CO;2, 2003.

Simpson, J., Kummerow, C., Tao, W.-K., and Adler, R. F.: On the Tropical Rainfall Measuring Mission (TRMM), Meteorol. Atmos. Phys., 60, 19–36, https://doi.org/10.1007/BF01029783,1996.

Sun, L. L. and Fu, Y. F.: A new merged dataset for analyzing clouds, precipitation and atmospheric parameters based on ERA5 reanalysis data and the measurements of the Tropical Rainfall Measuring Mission (TRMM) precipitation radar and visible and infrared scanner, Earth Syst. Sci. Data, 13, 2293–2306, https://doi.org/10.5194/essd-13-2293-2021, 2021.

Viltard, N., Kummerow, C., Olson, W. S., and Hong, Y.: Combined use of the radar and radiometer of TRMM to estimate the influence of drop size distribution on rain retrievals, J. Appl. Meteorol., 39, 2103–2114, https://doi.org/10.1175/1520-0450(2001)040<2103:Cuotra>2.0.Co;2, 2000.

Wang, Y., Fu, Y. F., Liu, G. S., Liu, Q., and Sun, L.: A new water vapor algorithm for TRMM Microwave Imager (TMI) measurements based on a log linear relationship, J. Geophys. Res., 114, D21304, https://doi.org/10.1029/2008JD011057, 2009.

Wu, Z. H. and Fu, Y. F.: A new dataset of rain cell generated from observations of the Tropical Rainfall Measuring Mission (TRMM) precipitation radar and visible and infrared scanner and microwave imager [Data set], Zenodo, https://doi.org/10.5281/zenodo.15387988, 2025.

Yokoyama, C., Zipser, E. J., and Liu, C.: TRMM-Observed shallow versus deep convection in the eastern pacific related to large-scale circulations in reanalysis datasets, J. Climate, 27, 5575–5592, https://doi.org/10.1175/JCLI-D-13-00315.1, 2014.

Yuter, S. E. and Houze, R. A.: Three-Dimensional kinematic and microphysical evolution of florida cumulonimbus. Part II: frequency distributions of vertical velocity, reflectivity, and differential reflectivity, Mon. Weather Rev., 123, 1941–1963, https://doi.org/10.1175/1520-0493(1995)123<1941:Tdkame>2.0.Co;2, 1995.

Zhou, Y., Lau, W. K. M., and Liu, C. T.: Rain characteristics and large-scale environments of precipitation objects with extreme rain volumes from TRMM observations, J. Geophys. Res.-Atmos., 118, 9673–9689, https://doi.org/10.1002/jgrd.50776, 2013.

Zipser, E. J. and Lutz, K. R.: The vertical profile of radar reflectivity of convective cells: A strong indicator of storm intensity and lightning probability?, Mon. Weather Rev., 122, 1751–1759, https://doi.org/10.1175/1520-0493(1994)122<1751:Tvporr>2.0.Co;2, 1994.